Research Article

Effects of Pulsed Laser Repetition Rate and Duty Cycle on Heat-Affected Zone Narrowing in Laser Powder Bed Fusion of 316L Stainless Steel

Sukunya Pathompakawant and Pruet Kowitwarangkul*
The Sirindhorn International Thai-German Graduate School of Engineering (TGGS), King Mongkut's University of Technology North Bangkok, Bangkok, Thailand

Patiparn Ninpetch
Department of Industrial Engineering, Faculty of Engineering, Rajamangala University of Technology Thanyaburi, Pathum Thani, Thailand

Somboon Otarawanna
National Metal and Materials Technology Center (MTEC), National Science and Technology Development Agency (NSTDA), Pathum Thani, Thailand

* Corresponding author. E-mail: pruet.k@tggs.kmutnb.ac.th DOI: 10.14416/j.asep.2025.03.007
Received: 19 September 2024; Revised: 13 November 2024; Accepted: 28 January 2025; Published online: 25 March 2025

Abstract
Laser Powder Bed Fusion (L-PBF) is a type of metal additive manufacturing process. It has attracted increasing interest over the past few decades. L-PBF systems typically use continuous wave (CW) emission. Recently, pulsed wave (PW) emission has been introduced in order to have better control of the heat-affected zone (HAZ) and potentially enhance spatial resolution. Generally, the PW emission involves the laser temporal profile that can be modulated by such as pulse durations, duty cycles, and pulse repetition rates (PRR). Nevertheless, based on a literature survey, the systematic investigation of pulsed wave (PW) emission in the L-PBF process, which changes the laser temporal profile by adjustment of the pulsed laser parameters has scarcely been examined. The determination of suitable pulsed laser parameters needs to be employed in order to achieve these good attributes of PW emission to obtain the final part with high quality. Hence, this work investigates the effects of modifying the pulsed laser parameters on single track formation in AISI 316L pulsed L-PBF using numerical simulation with Flow-3D AM Software. The simulation cases used different pulse durations, duty cycles, and pulse repetition rates (PRR) while the layer thickness, scanning speed and laser power were kept constant. The key results demonstrate that increasing the PRR by four times while maintaining a constant Linear Energy Density (LED) reduced the width of the 700 K isotherm HAZ by 7%, highlighting the role of PRR in minimizing thermal diffusion. Furthermore, increasing the duty cycle while keeping the PRR and pulse period constant resulted in a smoother surface finish, as evidenced by a reduction in surface roughness (Ra) to less than 4 µm, compared to typical Ra values of 5–12 µm in CW L-PBF systems. This change also resulted in a wider HAZ, emphasizing the trade-off between surface finish and thermal diffusion. The findings from this study provide insights for optimizing processing parameters in L-PBF with PW emission, enabling the production of parts with finer geometries and enhanced surface quality.

Keywords: Additive manufacturing, AISI 316L, CFD, HAZ, L-PBF, Pulsed wave emission

1 Introduction

The Laser Powder Bed Fusion (L-PBF) process is a branch of an additive manufacturing (AM) technique employing laser as the heat source to selectively melt the metal powder bed under a controllable environment [1]. This process enables the creation of 3D objects through a layer-by-layer approach to obtain the desired geometry outlined in the 3D computer-aided design (CAD). The significant advantage of the L-PBF process is the production of complex-shaped metal parts that were previously difficult to produce with traditional manufacturing processes, reflecting the rapid advancements and innovative potential of AM technologies [2], [3]. The manufacturing process of 3D-printed components using the L-PBF process involves the utilization of a laser such as Ytterbium (Yb) fiber laser and Nd: YAG, which can operate in two distinct modes: continuous wave (CW) and pulsed wave (PW) emissions [4]. The use of PW emission has been beneficial for controlling the heat-affected zone (HAZ) which in turn influences the microstructure and thermal stresses, thereby enhancing spatial resolution and achieving finer details in L-PBF. However, it can also produce negative effects, such as lack of fusion and high surface roughness (Ra) [5]–[8]. The distinction between both laser types lies in their emission patterns. CW emission delivers light continuously at a consistent power level whereas PW emission emits light in short, regulated intervals, achieving high peak power with periods of no light emission between these pulses. In contrast to those of CW, pulsed laser parameters are more intricate and involve variables such as duty cycle, pulse duration, and pulse interval. Therefore, understanding the complexity of process parameters in metals produced by pulsed L-PBF presents a significant challenge. These laser emission modes can affect temperature field and output characteristics such as melt pool size, deposited track size, HAZ and Ra. Understanding the impact of each laser mode is crucial for optimizing the L-PBF process and achieving desired part properties [5], [9].

CW emission has generally been a typical choice in L-PBF applications. Several studies [10]–[12] have focused on the influence of process parameters on the quality of single tracks in L-PBF. Gunenthiram *et al*., [13] explored how laser power and speed affect stainless steel melt pools highlighting the importance of laser settings in improving part quality and consistency. Similarly, research by Adjamsky *et al*., [14] highlighted the significance of scanning speed and laser power in determining track morphology. A study by Xu *et al*., [15] focused on single-track within selective laser melting of 316L stainless steel, employing three-dimensional numerical simulations to study grain growth. This study highlighted the importance of optimizing process parameters to achieve a uniform and finer grain structure, thus improving the mechanical properties of the manufactured parts.

In recent years, PW emissions have had an increasing trend for their application in manufacturing components [16]. Several studies have demonstrated that PW emissions in pulsed L-PBF offer effective control over the HAZ, which is crucial for creating detailed features like thin walls, lattice structures, and intricate geometries [8], [17]. For instance, Caprio *et al*., [18] conducted a comparative analysis between continuous and pulsed L-PBF in AISI 316L stainless steel, finding that continuous L-PBF generated larger melt pools and higher deposition rates, whereas pulsed L-PBF produced narrower tracks—ideal for precision-focused designs. Based on the literature review, it was found that Pulsed Laser Welding, and pulsed L-PBF have been extensively investigated experimentally across various metallic materials such as mild steel [9], AISI 316L [5], [6], [8], [19]–[22], AlSi10Mg and AlSi [18], [23], [24], Ni-Alloys [3], [7], [25]–[27] and Ti-Alloys (Ti6Al4) [28]–[31]. As mentioned earlier, the PW emission in pulsed L-PBF significantly affects the controlling of temperature distribution, HAZ, and melt pool behavior. These variables involved the complex physical phenomena during pulsed L-PBF such as heat transfer, fluid flow, phase transformation, and the Marangoni effect. Hence, understanding complex physical phenomena, and parameters' effects on temperature distribution, and melting pool behavior during pulsed L-PBF using numerical simulation is requisite, and challenge. Numerical simulation is an essential tool for modeling complex physical phenomena in both CW and PW emissions processes. The literature revealed that there are many studies that utilize numerical simulation to study and elucidate complex physical phenomena in CW emission processes. Ninpetch *et al*., [32] explored the characteristics and dynamics of thermal fluids in continuous L-PBF, emphasizing how variations in powder layer thickness and energy input application influence the development of a single track. Based on our literature review, applying numerical simulation to analyze thermal behavior and melt pool morphology

in pulsed L-PBF has conducted relatively few. Ding *et al*., [22] conducted a comparative study of CW and PW emissions in the L-PBF process using both 3D numerical simulation and experimentation in AlSi10Mg on a Renishaw AM250 SLM machine. Their results suggested that CW emission led to larger, ellipse-shaped molten pools with finer grains due to rapid cooling whereas PW emission resulted in smaller, comet-shaped pools. Additionally, Bayat *et al*., [33] developed a numerical model to examine the impact of laser cycle duration on melt pool dynamics in pulsed laser welding of AISI 316L. They found that longer laser cycles generated larger melt pools and distinctive track morphologies.

This scarcity of numerical research emphasizes the need for studies that apply numerical simulation to analyze thermal behavior and melt pool morphology in pulsed L-PBF. Numerical simulations provide distinct advantages, enabling detailed insights into the thermal and structural dynamics of complex processes like PW emission in L-PBF. This study seeks to address these research gaps, offering a comprehensive computational approach to understand the impact of pulse duration, duty cycle, and pulse repetition rate (PRR) on single-track formation in AISI 316L. Therefore, this study performed numerical simulations of pulsed L-PBF to study the effects of pulsed laser parameters, including pulse duration, duty cycle, and pulse repetition rate (PRR), on single-track formation in AISI 316L. The results focus on melt track morphology and geometrical dimensions, e.g. melt pool dimensions, surface roughness and HAZ.

2 Materials and Methods

2.1 *Numerical modeling*

This study employed computational fluid dynamics (CFD) simulation by using FLOW-3D AM software, developed by Flow Science, Inc., to model the L-PBF process with CW and PW emissions. The modeling framework was structured into two main parts, as illustrated in Figure 1. The first part is related to the preparation of the powder bed, encompassing the metal powder spreading and settling processes. This part models the particle movement using the discrete element method (DEM), with a color bar indicating the powder diameter size ranging from 0.0025 mm to 0.003 mm for clarity. The second part investigates the melting process, exploring various physical phenomena through conservation equations, the moving laser heat source model, the Marangoni effect, recoil pressure, and solidification enthalpy [34]–[36]. The color bar in this section represents the temperature distribution within the melt pool, ranging from 298 K (blue) to 1800 K (red), providing a visual depiction of the thermal gradient during the melting process. The laser beam was represented by a Gaussian distribution.

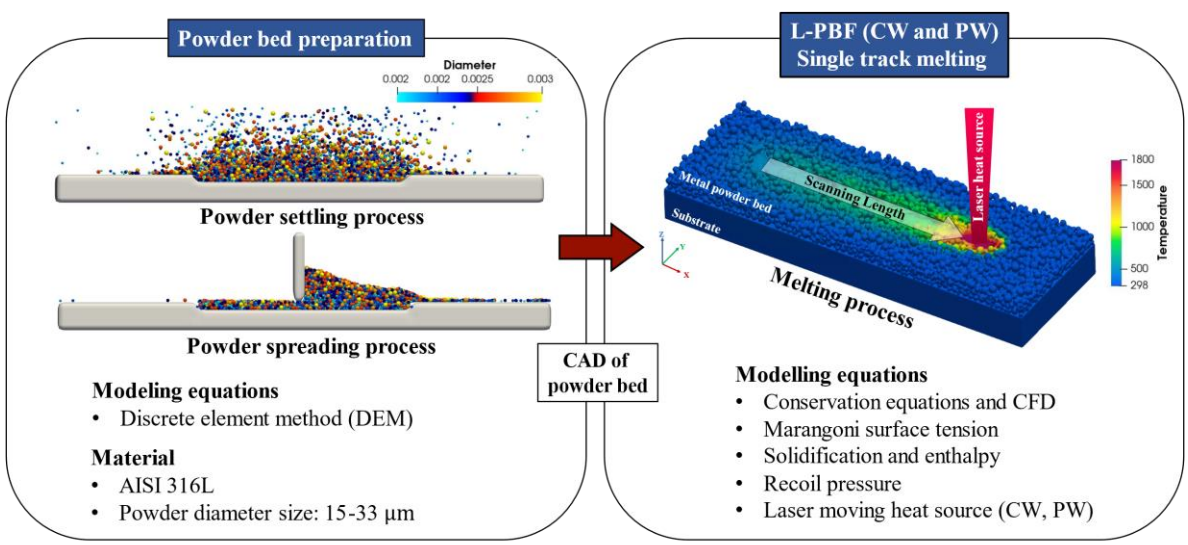

Figure 1: The modeling framework of L-PBF process.

2.2 *Powder bed generation*

The DEM was used to simulate the creation of a metal particle bed on a solid substrate, focusing on particle movement, inter-particle interactions, and interactions between particles and the walls. In this study, metal particles were modeled as perfect spheres with varying radii. Both the wall and the substrate were treated as rigid bodies. Velocities of each metal particle in the x, y, and z directions, accounting for both translational and rotational motion were calculated by solving Newton's second law with DEM. The inter-particle interaction models are detailed in the following Equations (1)–(3) [37]:

$$F_{n\,i} = -k_s\, d\!l\!n - \eta_n\,(u' \cdot n)\, n \tag{1}$$

Inter-particle force in tangential direction:

$$F_{n\,i} = -\eta_t (u' - (u' \cdot n)\, n) \tag{2}$$

Total particle interaction force:

$$l\!\!\!^{-}_0 = r_i + r_j;\;\; l\!\!\!^{-} = x_j - x_i;\; d\!l\!\!\!^{-} = l\!\!\!^{-}_0 - l\!\!\!^{-};\; n = \frac{1}{l\!\!\!^{-}};\; u' = u_j - u_i \tag{3}$$

where x_i denotes a coordinate vector of an individual particle center, r_i is particle radius, k_s is spring constant, u_i is particle velocity vector, and η is drag coefficient.

2.3 *Heat transfer and melt flow dynamic*

The L-PBF process involves a variety of complex physical phenomena, including heat transfer and fluid dynamics. These phenomena are governed by the fundamental conservation equations of mass, energy, and momentum shown in Equations (4)–(6), respectively [34], [35], [37].

$$\frac{\partial \rho}{\partial t} + \nabla.(\rho \vec{v}) = 0 \tag{4}$$

where $\vec{v}$ and ρ are the velocity and density of liquid metal, respectively.

The formulation of the energy conservation equation is shown in Equation (5)

$$\frac{\partial H}{\partial t} + (\vec{v}.\nabla)H = \frac{1}{\rho}.(\nabla.k\nabla T) + Q_{laser} \tag{5}$$

Where H represents the enthalpy, k denotes the material's thermal conductivity, T signifies the temperature and Q_{laser} is heat source

The momentum conservation equation is as follows [35].

$$\frac{\partial \vec{v}}{\partial t} + \vec{v}.\nabla\vec{v} = \frac{1}{\rho}.(\mu\nabla^2 - \nabla p\vec{v}) + \vec{g} + \overrightarrow{F_B} \tag{6}$$

where μ represents the viscosity of liquid metal, p stands for pressure, t is time, $\vec{g}$ is the gravitational acceleration, and $\overrightarrow{F_B}$ is the buoyancy force, which can be determined by Equation (7).

$$\overrightarrow{F_B} = \vec{g}\beta(T - T_m) \tag{7}$$

where β represents the thermal expansion coefficient of liquid metal, T is temperature, and T_m is the liquidus temperature.

The Marangoni effect is the occurrence associated with mass transfer along the surface of the melt pool caused by the surface tension gradient. This effect significantly impacts the surface morphology of the molten pool and heat convection in the molten pool. The surface tension model with temperature dependence is presented by Equation (8).

$$\gamma(T) = \gamma_o + \frac{d\gamma}{dT}(T - T_m) \tag{8}$$

where γ indicates the surface tension at temperature, γ_o is the surface tension at the melting temperature, T_m denotes the melting temperature and $\frac{d\gamma}{dT}$ represents the surface tension coefficient with temperature dependence.

Additionally, the surface morphology of the molten pool was reconstructed and accurately captured using the volume of fluid (VOF) method. This method determines the evolution of the free surface by solving Equation (9) [38].

$$\frac{\partial F}{\partial t} + \nabla\cdot(\vec{v}F) = 0 \tag{9}$$

A cell is considered void when $F = 0$, and completely filled with fluid when $F = 1$. If F falls between 0 and 1, this indicates the presence of an interface between the fluid and the void within the cell.

The mechanism of recoil pressure is applied to detail the flow behavior of liquid metal at the surface, specifically when the molten pool surface temperature surpasses the boiling threshold. The recoil pressure is defined in Equation (10) [32], [36].

$$P_r = 0.54 P_0 exp\left(\Delta H_v \frac{T-T_b}{RTT_b}\right) \quad (10)$$

where P_0 represents the saturation pressure, ΔH_v denotes the enthalpy of metal vapor, R is gas constant and T_b refers to the boiling temperature of the material.

2.4 *Laser heat source*

During the L-PBF process with a typical CW emission, the Gaussian distribution (Equation (11)) was typically used to model as the moving laser heat source above the metal particle bed.

$$Q = \frac{\eta P_{Laser}}{\pi R_s} exp\left(-\frac{(x-x_s)^2+(y-y_s)^2}{R_s^2}\right) \quad (11)$$

where Q_{laser} refers to the laser power, η is the absorption coefficient, P_{laser} is the laser power, D_s is the laser diameter, x_s and y_s are the coordinates of the laser beam's center.

In this study, the simulation employed a pulsed laser as shown in Figure 2, with the pulsing theory adapted from previous studies on PL-PBF [5], [20]. The calculations for the PL-PBF process were conducted using Equations (12)–(16).

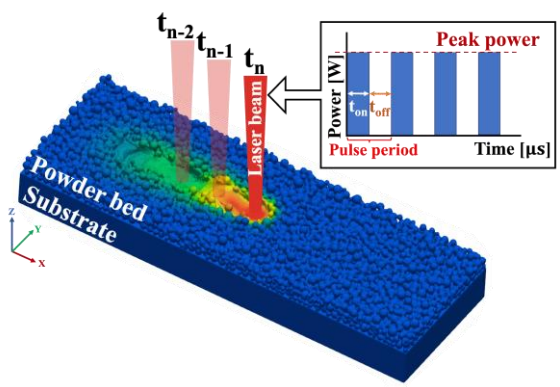

Figure 2: Simulation geometry and process parameters.

As the laser power input was modulated in one of the conditions to ensure consistent energy density, the scan speed was adjusted accordingly using the following equation [20].

$$v_{PW} = \frac{P_{avg}(\delta)}{P_{CW}} v_{CW} \quad (12)$$

The process parameters used to compare single-track deposition under different emission modes are the scanning speed (v) and average power output (P) of the laser beam. In Equation (12), the subscripts 'PW' and 'CW' denote the respective emission modes. P_{CW} represents the instantaneous power output of the laser source during continuous wave emission while P_{avg} signifies the average power delivered during modulated emission [5].

An important parameter related to the PW emission characteristics is the duty cycle which is defined by Equation (13)

$$\delta = t_{on} \cdot PRR \quad (13)$$

where t_{on} is the pulse duration and PRR is the pulse repetition rate. PRR is further defined by:

$$PRR = \frac{1}{t_{on} + t_{off}} \quad (14)$$

where t_{off} refers to the laser-off time between consecutive pulses. The lower values of the duty cycle indicate a larger temporal spacing between consecutive pulses while the duty cycle of CW emission is 100%. Thus, the calculation of average power P_{avg} in PW emission is:

$$P_{avg} = E \cdot PRR. \quad (15)$$

While prior parameters detail the time-based characteristics of PW emission, the spatial aspect of pulse overlap (O_p) and laser spot overlap distance (S_{ov}) become crucial consideration, influenced by the point distance (d_p) parameter. For laser beam diameter (d_s), setting each pulse at a certain point distance (d_p) allows the computation of pulse overlap as follows.

$$O_p = \frac{S_{ov}}{d_s} = \frac{d_s - d_p}{d_s} \quad (16)$$

2.5 *Material properties and modeling parameters*

The AISI 316L material properties used in this study are detailed in Table 1 [39]–[41] and Figure 3, using data sourced from the datasheet in [42], Other modeling parameters used in the simulation are listed in Table 2, which were obtained from previous research in [43].

Table 1: Temperature-independent material properties of AISI 316L employed in this work [39]–[41].

Material Property	Value
Solidus temperature	1598 K
Liquidus temperature	1715 K
Evaporation temperature	3090 K
Viscosity	0.00345 Pa·s
Latent heat of fusion	2.7×10^5 J/kg
Latent heat of evaporation	7.45×10^6 J/kg

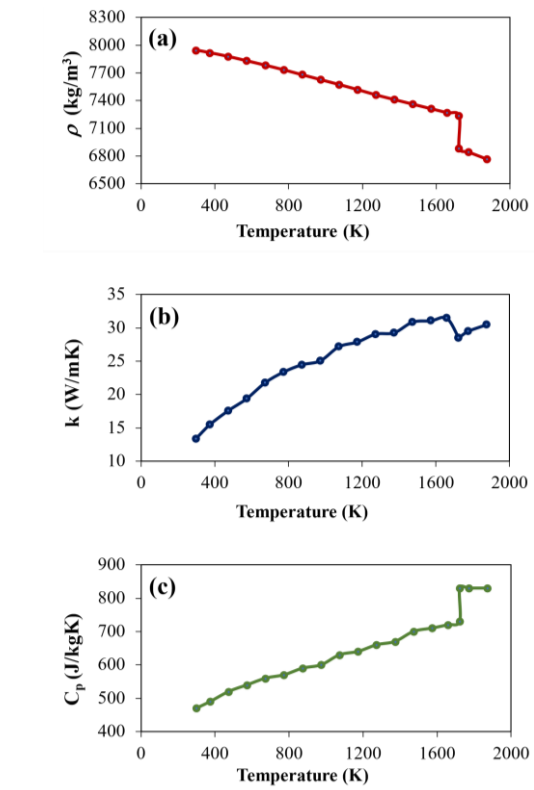

Figure 3: Temperature-dependent material properties of AISI 316L presented as line graphs, with data sourced from the datasheet in [42]. (a) Density, (b) Thermal conductivity, and (c) Specific heat.

Table 2: Parameters for the thermo-fluid flow model employed in this study [43].

Parameter	Value
Laser beam diameter	70 µm
Mesh size	4 µm
Atmospheric pressure	1.013×10^5 Pa

2.6 *Computational configuration*

To simplify the numerical model of the study, the following assumptions have been made: 1) the metal powders are spherical, 2) The molten metal flow is regarded as laminar flow, and 3) the molten metal is an incompressible Newtonian fluid. CFD simulations were performed in the FLOW-3D AM software suite to support Multiphysics modeling. All the simulations were performed on a computer equipped with an Intel Core i7-11700K processor and 64 GB RAM. The numerical modeling process began with the creation of a CAD model, in the STL format, representing the metal powder bed layer through the FLOW-AM software. The STL file depicting the metal powder bed was then imported into the FLOW-AM simulation program. This step enabled the analysis of temperature distribution, fluid flow dynamics and scanning track characteristics during the L-PBF process. The computational domain for both CW and PW melting processes (Figure 4(a)) has dimensions of 500 µm × 1500 µm × 180 µm (width × length × height) with a powder bed layer thickness of 50 µm. The metal powder comprised of particles sized between 15 µm and 33 µm. Both powder and substrate materials were AISI 316L.

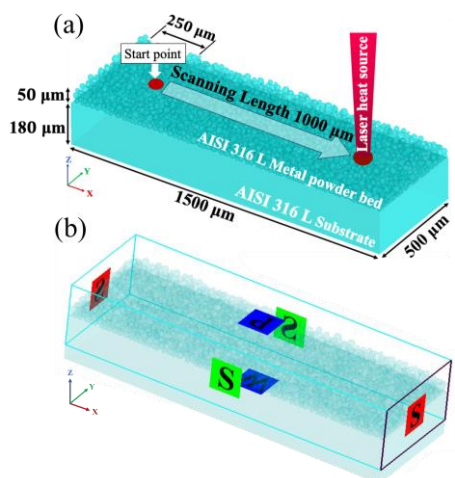

Figure 4: (a) The computational domain for both CW and PW melting processes and (b) Boundary conditions.

In this work, the computational mesh used consists of approximately three million elements with an element size of about 4 µm. Figure 4(b) also shows the boundary conditions. The heat convection and radiation were modeled on the upper surface. The void region above the layer of metal powder was subjected to atmospheric pressure and an initial temperature of 298 K (Z-max boundary). The bottom surface was treated as a wall with non-slip conditions (Z-min boundary) while the maximum and minimum boundaries in both the X and Y directions were

defined as symmetry boundary conditions. The laser beam size, layer thickness, scanning speed and laser power were set at 70 µm, 50 µm, 630 mm/s and 180 W, respectively. The six simulation cases were systematically designed to study the effects of laser parameters on melt pool behavior, with criteria based on variations in pulse duration, repetition rate, and duty cycle to address specific questions about how energy input and temperature distribution affect melt pool morphology. Specifically, cases (b), (c), and (d) focused on the impact of varying pulse duration, while cases (e), (c), and (f) were set up to analyze the effects of different duty cycles, with the Laser Energy Density (LED) calculated as the ratio of laser power (P) to scanning speed (v). The laser temporal profile and laser spot overlap of each case were illustrated in Figure 5. The figure shows the energy distribution of pulsed laser beams, with darker pink indicating overlapped higher energy density. As pulse t_{off} shortens, energy overlaps more, increasing cumulative heating. Longer t_{off} results in less overlap and lower energy concentration.

Table 3: Process parameters for each case in this study.

Case	Pulse Duration, t_{on} (µs)	Off Duration, t_{off} (µs)	Duty Cycle (%)	Period or Cycle Time (µs)	Pulse Overlap (%)	PRR (Hz)	Cycle (per mm)	LED (J/mm)
(a)	100 (CW)	-	100	-	-	-	-	0.28
(b)	25	25	50	50	63.3	20000	32	0.14
(c)	50	50	50	100	37.9	10000	16	0.14
(d)	100	100	50	200	5.3	5000	8	0.14
(e)	25	75	25	100	26.5	10000	16	0.07
(f)	75	25	75	100	46.3	10000	16	0.21

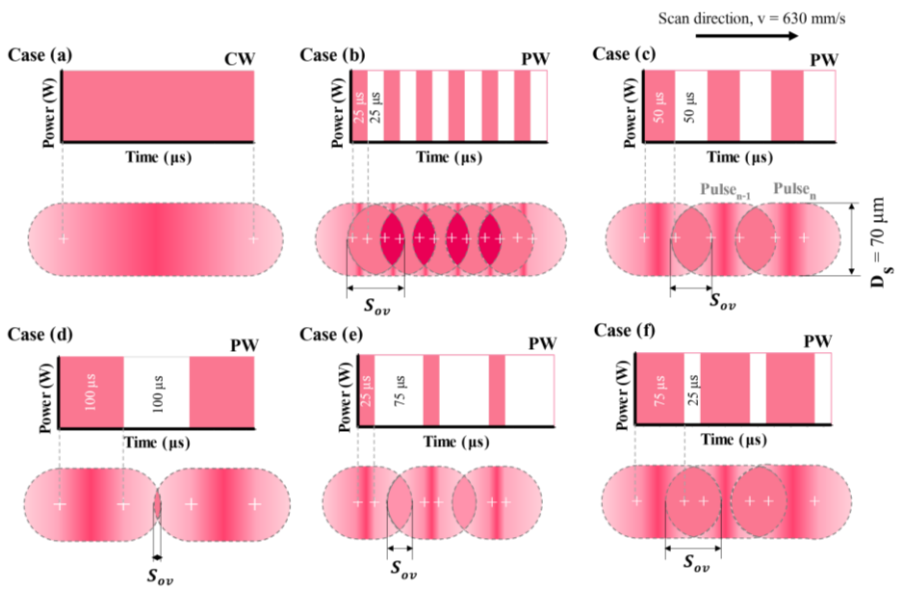

Figure 5: Laser temporal profile and laser spot overlap for each case in this study, with darker shades of pink indicating overlapped higher energy density.

3 Results and Discussion

3.1 *Mesh Convergence Analysis*

Mesh convergence analysis was a critical step to ensure the reliability and accuracy of the model, as well as to determine the optimal mesh size for this study. An analysis was conducted on six mesh sizes:10, 8, 6, 5, 4.5, and 4 µm, corresponding to approximately 0.21, 0.42, 0.99, 1.71, 2.32, and 3.32 million elements, respectively. The analysis focused on the melt pool depth in single-track melting. As shown in Figure 6, the melt pool depth graph began to converge and stabilize at a mesh size of 5 µm or finer, with the melt pool depth stabilizing at a value of 85µm, indicating that further decreasing the mesh size

did not significantly affect the results. However, reducing the mesh size from 5 µm to 4.5 and 4 µm markedly increased computational time from 441 minutes to 1,913 and 2,354 min, respectively, although this remained within an acceptable time for this study. While a mesh size of 5 µm was considered sufficient for reliable predictions [44], a finer mesh size of 4 µm was employed to achieve maximum resolution. This size also aligns with the mesh used in the reference paper for validation in this study [43].

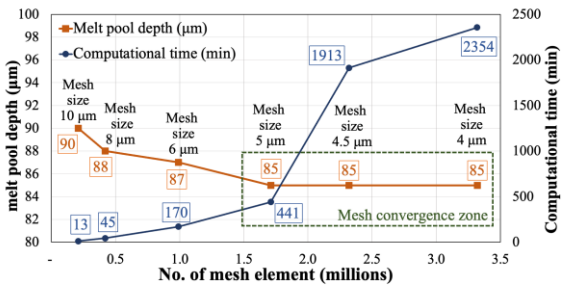

Figure 6: Results of the mesh convergence analysis in this study.

3.2 *Validation of numerical modeling*

The model validation process in this study consists of two parts. The first part involves validating the numerical model by comparing the melt pool shape and dimensions with experimental results from Pham *et al*., [43] and simulation results from Feng *et al*., [15]. The second part focuses on benchmarking the validated results against previous studies to identify trends. The study by Pham *et al*., focuses on the melt pool morphology in the L-PBF process for 316L stainless steel, providing detailed experimental data on melt pool dimensions, which serve as a benchmark for validating numerical simulations. Meanwhile, Feng *et al*., work [15] involves numerical simulation of the L-PBF process, offering a relevant reference for comparing simulation accuracy. The comparison revealed that the melt pool width and depth obtained in this study are consistent with the experimental results from Pham *et al*., [43] with a minor difference of approximately 4.14% for width and 5.56% for depth as shown in Figure 7. Additionally, the numerical results of the study were compared to Feng *et al*., simulation data, showing a minor difference of 2.03% for width and 2.35% for depth.

To ensure the reliability of the validation process, the results of this study were compared with other published works to verify their consistency. In this study, using a laser power of 180 W and a scanning speed of 630 mm/s (LED = 0.29 J/mm), the melt pool dimensions were determined to be 85 µm in depth and 145 µm in width. These findings were further analyzed by benchmarking them against the work of Zilong *et al*., [45]. Zilong *et al*., reported smaller melt pool dimensions (~60 µm depth and ~100 µm width) at a scanning speed of 1,470 mm/s (LED = 0.18 J/mm), attributed to reduced interaction time between the laser and the material. Conversely, they observed larger melt pool dimensions (~80 µm depth and ~125 µm width) at a slower scanning speed of 870 mm/s (LED = 0.3 J/mm), which corresponded to increased energy density and prolonged interaction time. The results of this study closely align with the experimental and simulation data reported by Zilong *et al*., demonstrating consistency with the observed trends in melt pool morphology under varying laser processing parameters. This comparative analysis validates the accuracy of the numerical model in predicting the shape and dimensions of the melt pool across diverse process conditions. Furthermore, these findings reinforce the model's potential applicability for advancing future research.

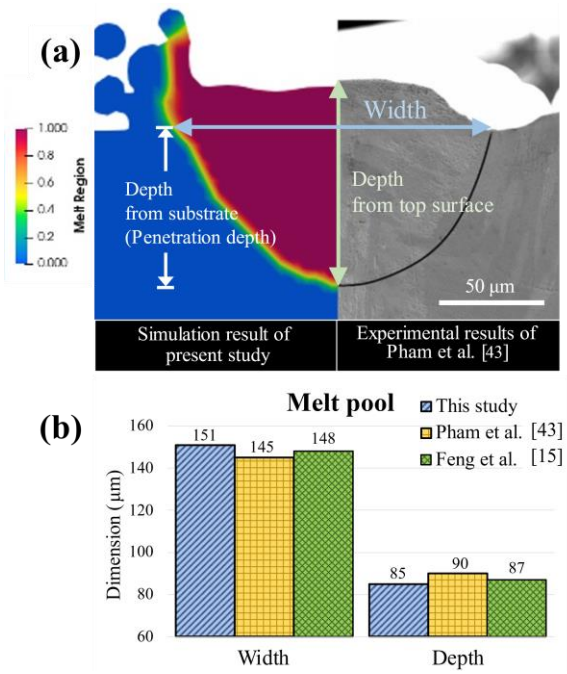

Figure 7: Comparison of the melt pool dimensions obtained in this study with the experimental results from Pham *et al*., [43] and the simulation results from Feng *et al*., [15]: (a) Melt pool shape and dimensions, (b) Melt pool width and depth at the top surface.

3.3 *Effect of laser parameters on melt track morphology and temperature distribution*

The melt track morphology and temperature results in the longitudinal cross-section are illustrated in Figure 8. The CW (case A) and PW with a high duty cycle of 75% (case F) led to higher heat accumulation corresponding with the results in [46]. Considering the depth in the region with temperatures of 1000–1200 K from the top surface of the substrate layer revealed a depth exceeding half of the substrate thickness. This was attributed to the relatively high LED values of 0.21 and 0.28 J/mm, respectively.

In contrast, case (e) exhibits the least intensity and shallowest heat distribution, with an LED value of 0.07 J/mm. Tracing the depth of the 1000–1200 K temperature zone reveals that the heat distribution did not penetrate down to the substrate layer much. Cases (b), (c), and (d), which all have LED values of 0.14 J/mm, exhibit similar temperature distributions with only subtle differences observed among them. Specifically, case (b), characterized by the highest PRR, exhibits a slightly deeper 1000–1200 K temperature distribution centered compared to cases (c) and (d). The quantitative results will be shown by melt pool depth in section 3.4. The obvious difference in melt pool shape between the end of t_{off} and t_{on} was evident in case (d), which has the least pulse overlap and the longest period. A flat surface appears at the end of t_{off} while a keyhole appears at the end of t_{on}.

The variation in temperature profiles across these images demonstrates how the laser's on/off cycling influences melt pool shape and temperature distribution in each case. These heat fluctuations control localized heating and cooling, affecting solidification rates and thermal gradients, which shape the melt pool boundaries and potentially impact the material's grain structure. Significant differences in temperature gradients and melt pool shapes were observed between continuous and pulsed modes, as well as among different pulsed settings, underscoring the role of process parameters such as pulse duration, duty cycle, and pulse repetition rate (PRR). These parameters directly affect thermal distribution, melt pool morphology, and surface roughness.

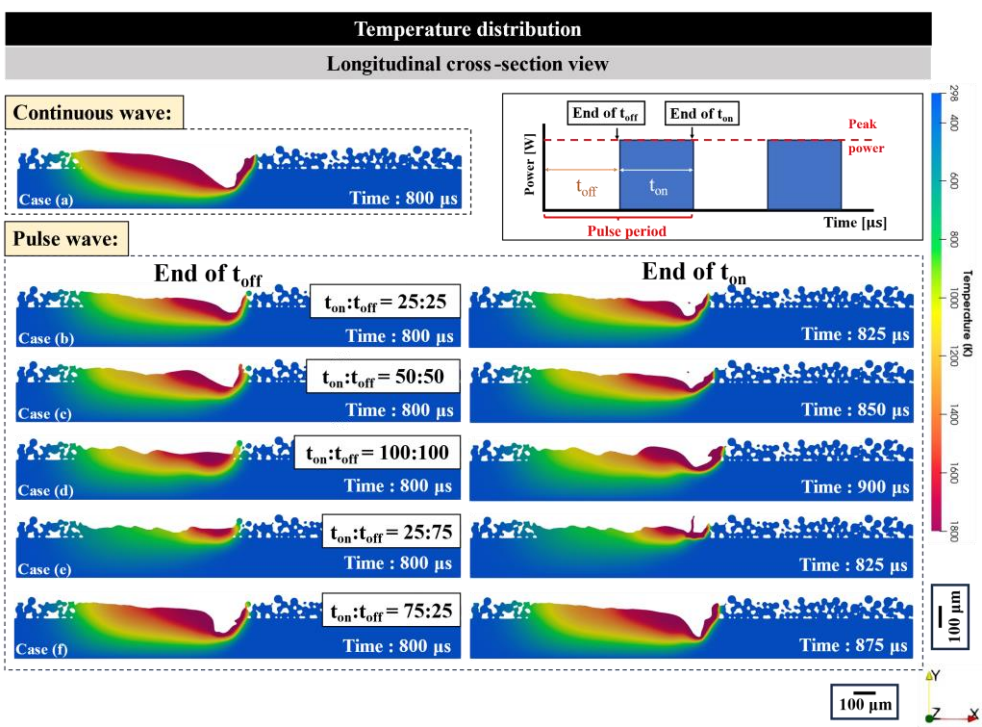

Figure 8: Melt pool shape and temperature distribution in the longitudinal cross-sectional view for each case.

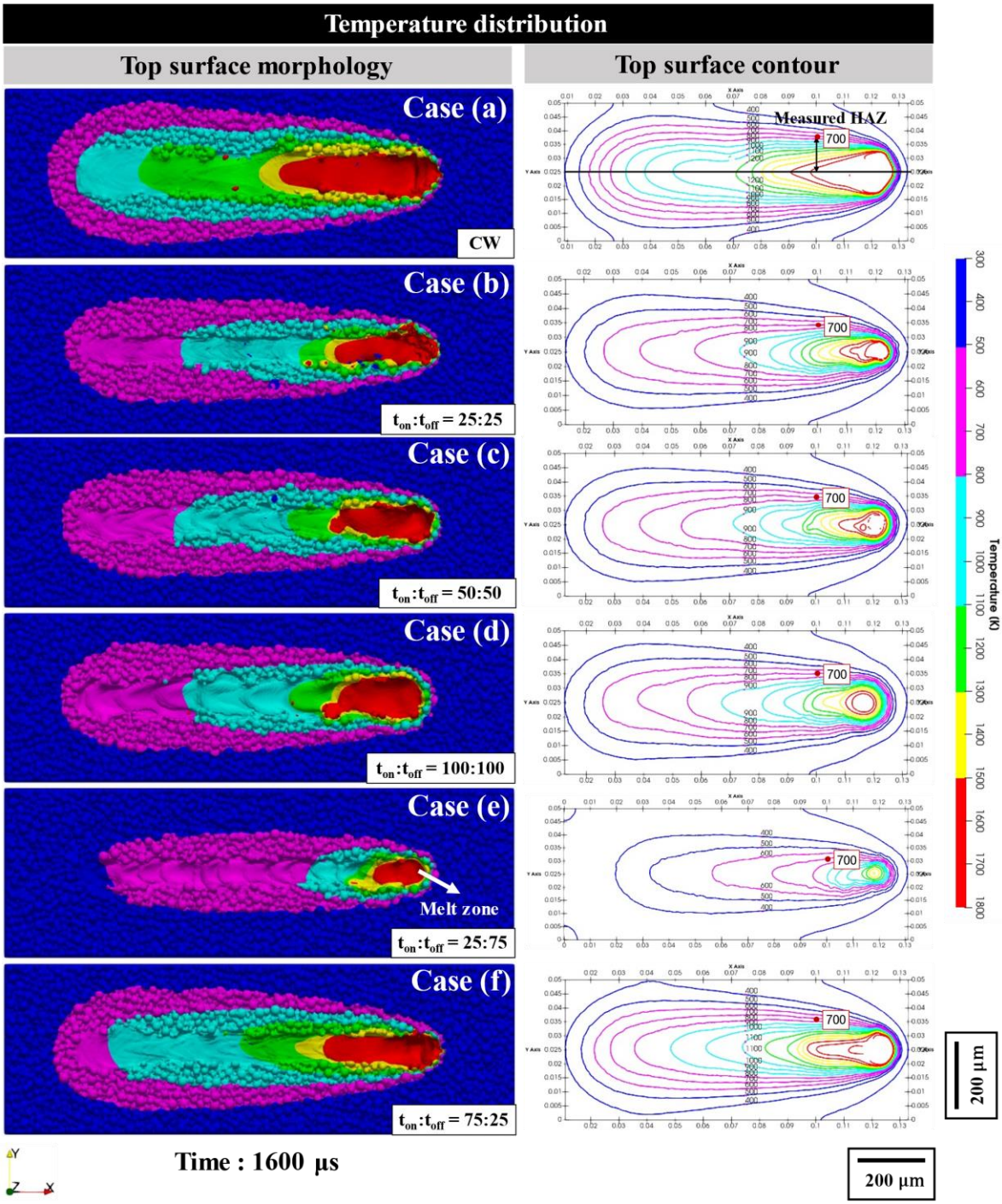

Figure 9: Melt pool shape and temperature distribution on the top surface.

Figure 9, cases (a)–(f), shows the temperature distribution and the HAZ with distances measured from the centerline to the 700 K isotherm. The HAZ, with temperatures ranging from 700 K to the melting point of 1715 K, was the region where various phenomena can occur, such as thermal stress, microstructure changes, grain growth, recrystallization, chromium-rich phase formation, and oxidation, etc. [43], [47], [48]. Additionally, measuring at this temperature allows for precise analysis of heat distribution in the HAZ, facilitating better control over laser parameters and minimizing undesired microstructural changes. Measuring the spread of heat between the 700 K contour line and centerline at position x equals to 0.1 cm, as depicted in Figure 8, reveals that in cases (b)–(d), which have equal LED values of 0.14 J/mm and the same duty cycles, adjusting the pulse duration impacted the temperature distribution. Specifically, case (b) exhibits a slightly smaller HAZ compared to cases (c) and (d), as demonstrated by the values in Figure 10. This indicates that shorter pulse durations, higher pulse repetition rates, and greater pulse overlap are associated with smaller HAZ, as they concentrate the heat input within a localized region and reduce thermal diffusion into surrounding areas. The focused energy input limits the melt pool width, confining the HAZ to a smaller zone. Specifically, discusses the foundational principles of laser-material interaction, highlighting the role of pulse overlap in minimizing thermal gradients and improving energy efficiency [49]. Additionally, demonstrates that optimizing energy density effectively controls melt pool morphology and reduces HAZ size [50], while emphasizing how higher pulse repetition rates enhance energy concentration and further restrict thermal diffusion [51]. The positive temperature dependence of the thermal conductivity in AISI 316L facilitates rapid heat dissipation at higher temperatures, further contributing to the reduction of the HAZ.

In cases (a), (c), (e), and (f), which represent the group with varying duty cycles, it was observed that a higher duty cycle (case f) resulted in the laser being active for a larger portion of each cycle, delivering more continuous energy. This increased energy input led to greater heat input and, consequently, a larger melt pool. Correspondingly, the measured melt pool widths are shown in Figure 11. These measurements indicate that the size of the melt pool correlates directly with the duty cycle, where a higher duty cycle generally leads to wider melt tracks. This observation is consistent with findings from previous research [6], which also demonstrated a direct relationship between increased duty cycle and track width, confirming that pulse duration and duty cycle significantly influence melt pool morphology. While a higher duty cycle might be beneficial for ensuring the complete melting of the powder particles, it can also result in a larger HAZ. Conversely, a lower duty cycle limits the duration of laser exposure in each cycle, reducing the heat input and helping to minimize both the melt pool size and the HAZ.

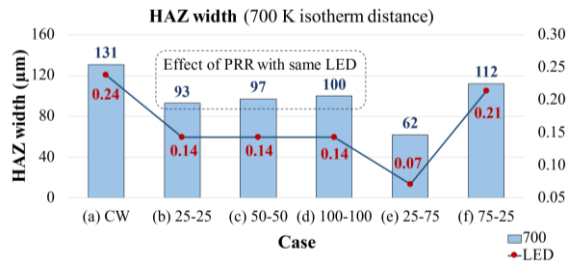

Figure 10: Comparison of the HAZ width and LED values between all six cases.

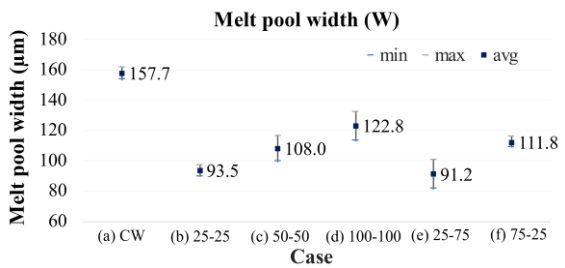

Figure 11: Comparison of the melt pool width values between all six cases.

3.4 *Effect of pulse period on surface roughness and shape of the melt pool*

The simulation results indicated that the forming quality of the single melt track varied, even when the same LED was applied. As illustrated in Figure 12 and described in Table 3, cases (b), (c), and (d) all employed a duty cycle of 50% and an LED of 0.14 J/mm². Noticeable differences in the top surface morphology and roughness of the longitudinal cross-sectional views were observed in Figure 12, cases (b)–(d), which were attributable to variations in laser pulse duration. Specifically, Figure 12, case (b), which represents a pulse period of 50 μs, exhibits a smoother top surface and bottom interface of the melt pool than

those seen in Figure 12, cases (c) and (d). This smoother surface and interface resulted from the shorter period and reduced exposure time to laser energy, leading to decreased localized heat accumulation and, consequently, a more stable melt pool. The differences in pulse periods among cases (b), (c), and (d) (50 μs, 100 μs, and 200 μs, respectively) resulted in distinct melt pool characteristics. Case (b), with the shortest pulse period (25 μs t_{on} and t_{off}), allows for more frequent energy input, producing a smoother surface morphology and resulting in lower Ra values of 3.62 μm on the top surface and 3.92 μm at the bottom interface. This smoothness is due to consistent heat distribution and stable melt pool formation. In contrast, case (d) with the longest pulse period (100 μs t_{on} and t_{off}) shows more pronounced surface irregularities, caused by longer intervals between pulses that allow for localized heat accumulation and stronger Marangoni-driven flow. This results in a rougher surface with Ra values of 6.93 μm. Case (c), with an intermediate pulse period, yields surface roughness values (4.36 μm on the top surface and 4.90 μm at the bottom interface) that fall between the other two cases.

In typical L-PBF processes using continuous wave lasers, Ra values of the final build part generally fall within the range of 5–12 μm, as reported in studies such as [1], [52], where Ra values around 7 μm were achieved. In our study, however, the single-track pulsed wave L-PBF demonstrated the potential to achieve lower Ra values, especially in case (b) where Ra reached approximately 3.6–3.9 μm. This lower Ra is attributed to the controlled heat input and reduced localized overheating provided by pulsed laser processing, which is advantageous for applications requiring smoother surfaces. The measured Ra values are shown in Figure 13(a).

The Marangoni effect, a surface tension-driven flow caused by temperature gradients in the melt pool, plays a significant role in pulsed laser processing [53]. For example, the long pulse duration in case (d), with a period of 200 μs (t_{on} = 100 μs and t_{off} = 100 μs), creates a strong temperature gradient, which intensifies Marangoni flows within the melt pool. This extended pulse period allows more localized heat to accumulate within the melt pool, leading to stronger Marangoni-driven flows that push molten material backward, causing a pronounced hump at the trailing edge of the melt pool. The humping effect generates due to the backward flow of molten metal, leading to the accumulation of material at the hump surface [53]. The larger hump in case (d) results from prolonged exposure to laser energy, which not only increases heat accumulation but also allows more time for the molten material to flow and form a raised surface. This wave-like pattern is caused by the intermittent nature of pulsed energy, where each "hump" corresponds to a pulse cycle, resulting in a periodic undulation that resembles a series of waves or beads along the melt track. These humps, driven by the Marangoni effect and thermal gradients, directly influence the surface roughness (Ra) values. In cases (b) through (d), increasing the pulse duration leads to higher Ra values on both the top surface and the bottom interface. For case (b), the Ra value is minimized due to the continuous energy delivery, while in case (d), the Ra value significantly increases because of the extended intervals between pulses. This allows the formation of a more pronounced hump driven by the Marangoni effect, resulting in a rougher surface. Specifically, case (b) has an Ra value approximately 37% lower than that of case (d).

Figure 13(b) shows the depth and the depth-to-width (D/W) ratio of the melt pool for cases (b)–(d). It should be noted that, in sections 3.4 and 3.5, the depth was measured from the substrate interface to the bottom of the melt pool, also known as the penetration depth. The results indicate that shorter t_{on} and t_{off} durations in case (b) led to a deeper melt pool compared to case (d). This relationship was opposite to that of the melt pool width, as shown in Figure 10. The D/W ratio is a critical parameter for classifying the melt pool regime, where values below 0.4 typically indicate conduction mode and values above 0.6 suggest keyhole mode [54]–[56]. In our study, case (b) maintained a D/W ratio of 0.4, reflecting a stable transition mode, which balances melt depth and width. Case (d), with a D/W ratio of 0.2, shifts towards conduction mode, which may limit the melt depth and could lead to incomplete layer fusion. These findings emphasize the importance of tuning pulse period and PRR to achieve desirable melt pool characteristics, particularly for pulsed wave L-PBF applications aimed at producing fine geometries and smoother surfaces.

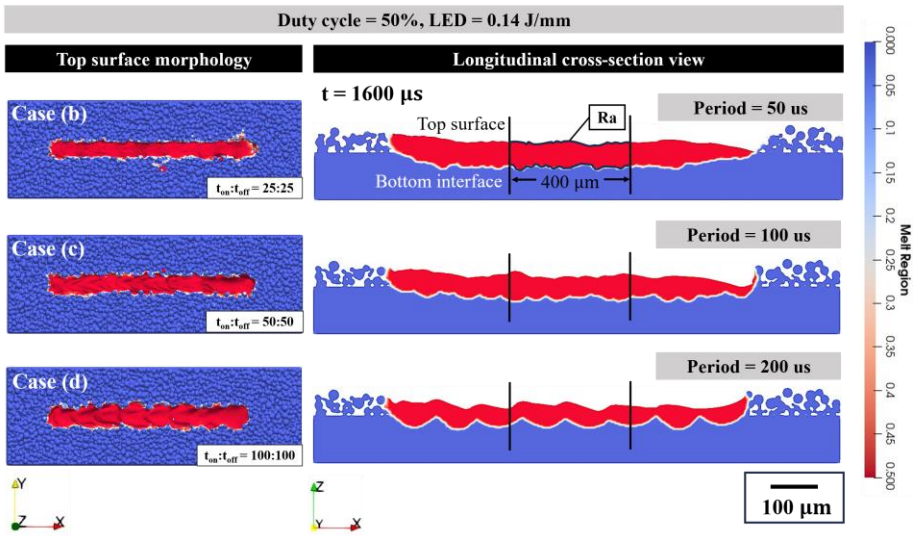

Figure 12: Comparison of melt pool on longitudinal cross-section view and the top surface of the case (b)–(d).

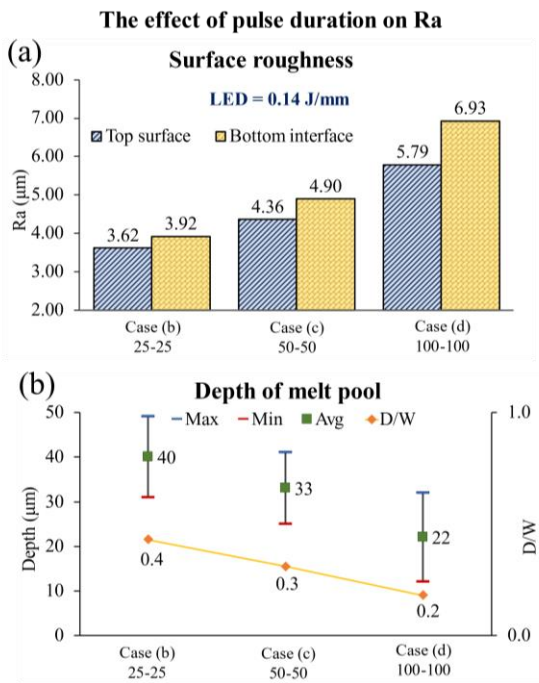

Figure 13: (a) Measured Ra of the top surface and bottom interface, (b) The penetration depth values and D/W ratio of the case (b)–(d).

3.5 *Effect of duty cycle and energy density on the surface roughness and shape of the melt pool*

Ra and D/W ratio of fabricated parts are significantly influenced by process parameters, particularly the duty cycle and LED. Achieving a low Ra is essential to minimize the need for post-process machining in the final build part, as highlighted in additive manufacturing studies [57]. Figure 14 shows the melt pool cross-sections for cases (e), (c), and (f), illustrating how variations in duty cycle and LED impact melt pool morphology.

In case (e), with the lowest duty cycle (25%) and LED of 0.07 J/mm, the short laser-on period (25 µs) combined with a long laser-off period (75 µs) provided insufficient energy to fully melt the bottom interface. This resulted in a shallower melt pool with poor bonding between the particle layer and substrate, which can lead to mechanical weaknesses. Consequently, case (e) exhibited a relatively high Ra of 5.12 µm on the top surface, reflecting the irregular surface morphology from insufficient energy input.

In contrast, increasing the duty cycle and LED in cases (c) and (f) led to significant changes in melt pool characteristics. Case (c), with a duty cycle of 50% and LED of 0.14 J/mm, showed a more balanced melt pool depth and surface smoothness. As seen in Figure 15(a), the Ra values for case (c) were reduced to 4.36 µm on the top surface, indicating an improvement in surface quality due to increased energy density, which allowed for more stable Marangoni flows that smoothed the surface.

Case (f), with the highest duty cycle (75%) and LED of 0.21 J/mm, produced the deepest and widest melt pool among the three cases. The increased laser-on period (75 µs) provided enough energy to fully penetrate the substrate, creating strong bonding and the smoothest surface finish with a Ra of 3.14 µm on

the top surface. The higher energy input in case (f) intensified Marangoni-driven flows within the melt pool, which contributed to a reduction in surface roughness. The depth of the melt pool also increased substantially, reaching a depth of 67 µm as compared to 33 µm in case (c), as shown in Figure 15(b).

The D/W ratio provides further insight into the melt pool regime for each case. In Figure 15(b), case (e) does not achieve a measurable D/W ratio due to insufficient melting depth. In case (c), the D/W ratio was calculated at 0.31, reflecting a transition mode that balances depth and width. However, in case (f), the D/W ratio increased to 0.6, indicating a more favorable depth-to-width balance, which is suitable for achieving a keyhole effect. This deeper and more controlled melt pool in case (f) aligns with the objective of producing fine geometries with robust structural properties.

In summary, adjusting the duty cycle and energy density has a profound effect on melt pool morphology and surface quality. Lower duty cycles, as in case (e), result in inadequate energy delivery, leading to a higher Ra and shallow melt pools, while higher duty cycles in cases (c) and (f) produce smoother surfaces and deeper melt pools. When compared to the Ra values reported in previous studies by Ľuboš *et al*., [58] and Wenjia *et al*., [59], all cases in this research demonstrated consistently lower Ra values. The Ra values obtained in this study were measured from single tracks, reflecting the initial stages of the manufacturing process, whereas the benchmark studies measured Ra from fully fabricated parts, representing the final surface quality. A previous study [58] observed Ra values ranging from ~6–9 µm under standard L-PBF conditions, while Wenjia *et. al*., [59] achieved Ra values of ~4.5–9.5 µm by optimizing pulse period and energy density. In contrast, the use of a pulsed laser emission in the current study achieved Ra values in the range of 3–6 µm, specifically measured from single tracks, which remain within the acceptable range for high-quality part fabrication. These results underscore the critical importance of precise control over the duty cycle and pulse repetition rate (PRR), which effectively stabilized the melt pool and minimized surface defects. Furthermore, the findings highlight that efficient melt pool control during the early stages of the manufacturing process can significantly enhance surface quality and provide a strong foundation for optimizing the characteristics of final parts and advancing the L-PBF process for future applications.

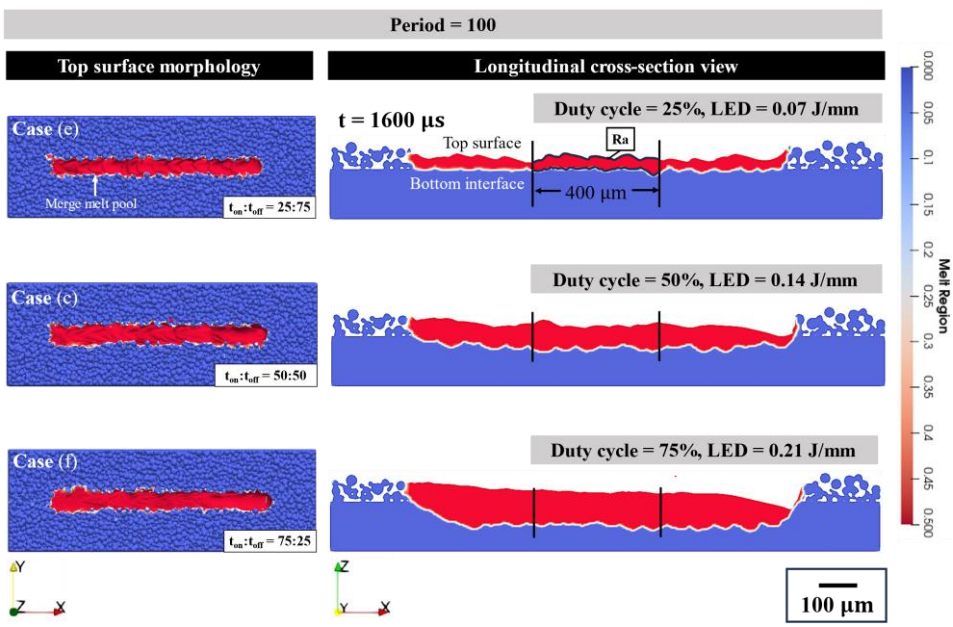

Figure 14: Comparison of melt pool on longitudinal cross-section view and the top surface of case (e), (c) and (f).

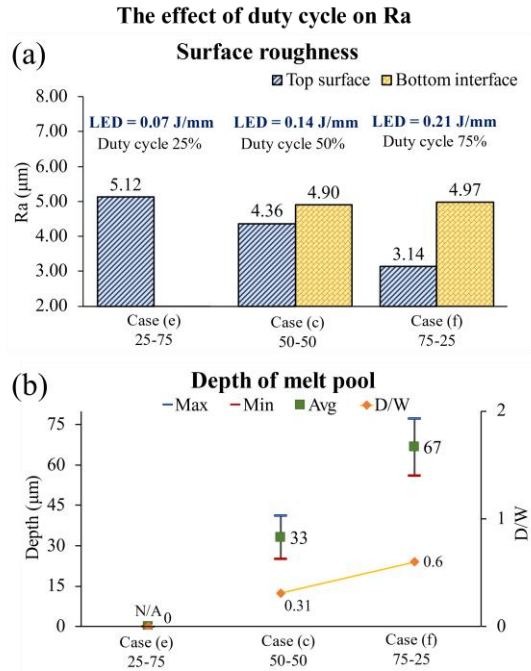

Figure 15: (a) Measured Ra of the top surface and bottom interface, (b) The penetration depth values and D/W ratio of case (e), (c) and (f)

4 Conclusions

This study presents a comprehensive numerical analysis of pulsed and continuous Laser Powder Bed Fusion (L-PBF) processes on single-track formation in 316L stainless steel, providing insights into the role of pulsed laser parameters in controlling melt pool characteristics. Key findings reveal that pulse repetition rate (PRR) and pulse period significantly impact heat distribution, melt pool morphology, and surface roughness (Ra). With a fixed duty cycle and laser energy density (LED), increasing PRR fourfold and reducing the pulse period narrowed the melt pool width by 24% and decreased the heat-affected zone (HAZ) width by 7%, highlighting the capability to achieve more precise and uniform melting. Additionally, a higher PRR combined with a shorter pulse period improved surface quality by reducing Ra by 37%, while lower PRR values led to uneven melting, increasing Ra and potentially causing incomplete melting in subsequent layers.

Adjusting duty cycle and LED further influenced melt pool dimensions and surface quality. High-duty cycle and LED reduced Ra but enlarged the HAZ and melt pool size, while a 25% duty cycle led to insufficient melting. The depth-to-width (D/W) ratio, a key metric for classifying melt pool regimes, was shown to be controllable by tuning pulsed laser parameters. For instance, a higher PRR and shorter pulse period shifted the melt pool from shallow conduction to a transition mode, while a high duty cycle led to keyhole formation, indicating a risk of defects. These findings demonstrate that PRR, pulse period, duty cycle, and LED can be strategically controlled to manage heat distribution, melt pool morphology, and Ra, enabling better control over HAZ and melt pool width—factors critical for fabricating fine geometries in additive manufacturing. The insights from this study contribute to a deeper understanding of pulsed laser parameter effects on 316L stainless steel processing, with practical implications for improving surface quality and structural integrity in high-precision applications.

The parts fabricated by the L-PBF process are generally produced layer-by-layer. Each layer bed is built in a track-by-track manner. Future work should be conducted on the impact of pulse duration, duty cycle, and pulse repetition rate (PRR) on multi-tracks formation and multi-layers formation and developed predictive models to facilitate the application of pulsed L-PBF in industrial-scale 3D printing.

Acknowledgments

This research budget was allocated by NSTDA-KMUTNB Collaborative Research and Development of High-Quality Post Graduate Scholarship (Contract No. Grad011/2564), and by National Science, Research and lnnovation Fund (NSRF), and King Mongkut's University of Technology North Bangkok (Project no. KMUTNB-FF-67-B-28).

Author Contributions

S.P.: conceptualization, methodology, software, validation, investigation, formal analysis, writing an original draft; P.K.: Supervision, Conceptualization, funding acquisition, formal analysis, methodology, investigation, writing an original draft, writing - reviewing & editing; S.O.: supervision, conceptualization, methodology, investigation, formal analysis, writing - review & editing; P.N.: investigation, writing - reviewing & editing. All

authors have read and agreed to the published version of the manuscript.

Conflicts of Interest

The authors declare no conflict of interest.

References

[1] J. P. Davim, Additive and Subtractive Manufacturing: Emergent Technologies. Berlin, Germany: *Walter de Gruyter GmbH*, pp. 1–289, 2019.

[2] S. A. Adekanye, R. M. Mahamood, E. T. Akinlabi, and M. G. Owolabi, "Additive manufacturing: The future of manufacturing," *Materiali in Tehnologije*, vol. 51, no. 5, pp. 709–715, 2017, doi: 10.17222/mit.2016.261.

[3] K. Mumtaz and N. Hopkinson, "Selective laser melting of Inconel 625 using pulse shaping," *Rapid Prototyping Journal*, vol. 16, no. 4, pp. 248–257, 2010, doi: 10.1108/13552541011049261.

[4] J. P. Davim, *Lasers in Manufacturing*. London, UK: ISTE Ltd and John Wiley & Sons, Inc, 2012, pp. 1–297.

[5] L. Caprio, A. G. Demir, and B. Previtali, "Influence of pulsed and continuous wave emission on melting efficiency in selective laser melting," *Journal of Materials Processing Technology*, vol. 266, pp. 429–441, 2019, doi: 10.1016/j.jmatprotec.2018.11.019.

[6] V. Laitinen, H. Piili, P. Nyamekye, K. Ullakko, and A. Salminen, "Effect of process parameters on the formation of single track in pulsed laser powder bed fusion," *Procedia Manufacturing*, vol. 36, pp. 176–183, 2019, doi: 10.1016/j.promfg.2019.08.023.

[7] A. Demir, P. Colombo, and B. Previtali, "From pulsed to continuous wave emission in SLM with contemporary fiber laser sources: Effect of temporal and spatial pulse overlap in part quality," *The International Journal of Advanced Manufacturing Technology*, vol. 91, pp. 2701–2714, 2017, doi: 10.1007/s00170-016-9875-5.

[8] A. B. Kaligar, H. A. Kumar, A. Ali, W. Abuzaid, M. Egilmez, M. Alkhader, F. Abed, and A. S. Alnaser, "Femtosecond laser-based additive manufacturing: Current status and perspectives," *Quantum Beam Science*, vol. 6, no. 1, p. 5, 2022, doi: 10.3390/qubs6010005.

[9] E. Assuncao and S. Williams, "Comparison of continuous wave and pulsed wave laser welding effects," *Optics and Lasers in Engineering*, vol. 51, pp. 670–680, 2013, doi: 10.1016/j.optlaseng.2013.01.007.

[10] Y. Guo, L. Jia, B. Kong, N. Wang, and H. Zhang, "Single track and single layer formation in selective laser melting of niobium solid solution alloy," *Chinese Journal of Aeronautics*, vol. 31, no. 4, pp. 860–866, 2018, doi: 10.1016/j.cja.2017.08.019.

[11] L. Wang, J. Han, and H. Ding, "Effects of different substrates on the formability and densification behaviors of cemented carbide processed by laser powder bed fusion," *Journal of Materials Processing Technology*, vol. 252, pp. 88–96, 2018, doi: 10.1016/j.jmatprotec.2017.09.026.

[12] J. J. S. Dilip, S. Zhang, C. Teng, K. Zeng, C. Robinson, D. Pal, and B. Stucker, "Influence of processing parameters on the evolution of melt pool, porosity, and microstructures in Ti-6Al-4V alloy parts fabricated by selective laser melting," *Journal of Materials Science*, vol. 52, no. 7, pp. 4117–4131, 2017, doi: 10.1007/s10853-017-0737-y.

[13] V. Gunenthiram, P. Peyre, M. Schneider, M. Dal, F. Coste, and R. Fabbro, "Analysis of laser–melt pool–powder bed interaction during the selective laser melting of a stainless steel," *Journal of Laser Applications*, vol. 29, no. 2, 2017, Art. no. 022303, doi: 10.2351/1.4983259.

[14] S. V. Adjamsky, Y. V. Tkachev, and G. A. Kononenko, "Effect of selective laser melting parameters on the melt pool formed by single tracks of the heat-resistant Inconel 718 nickel alloy," *Powder Metallurgy and Metal Ceramics*, vol. 59, no. 9–10, pp. 592–600, 2021, doi: 10.1007/s11106-021-00183-8.

[15] F. Xu, F. Xiong, M.-J. Li, and Y. Lian, "Three-dimensional numerical simulation of grain growth during selective laser melting of 316L stainless steel," *Materials*, vol. 15, no. 6800, pp. 1–27, Sep. 2022, doi: 10.3390/ma15196800.

[16] J. Beck, A. Schricker, C. Körner, and R. F. Singer, "Ultra-short pulsed laser powder bed fusion of Al-Si alloys: Impact of pulse duration and energy in comparison to continuous wave excitation," *Additive Manufacturing*, vol. 37, 2021, Art. no. 101631, doi: 10.1016/j.addma.2020.101631.

[17] X. Zhu, T. Yin, Y. Hu, S. Li, D. Wu, and Z. Xia, "Additive manufacturing of dense Ti6Al4V layer via picosecond pulse laser," *Materials*, vol. 16, no. 324, pp. 1–17, 2023, doi: 10.3390/ma16010324.

[18] L. Caprio, A. G. Demir, and B. Previtali, "Comparative study between CW and PW emissions in selective laser melting," *Journal of Laser Applications*, vol. 30, no. 3, 2018, Art. no. 032305, doi: 10.2351/1.5040631.

[19] C. A. Biffi, J. Fiocchi, P. Bassani, and A. Tuissi, "Continuous wave vs pulsed wave laser emission in selective laser melting of AlSi10Mg parts with industrial optimized process parameters: Microstructure and mechanical behaviour," *Additive Manufacturing*, vol. 24, pp. 639–646, 2018, doi: 10.1016/j.addma.2018.10.021.

[20] A. G. Demir, L. Mazzoleni, L. Caprio, M. Pacher, and B. Previtali, "Complementary use of pulsed and continuous wave emission modes to stabilize melt pool geometry in laser powder bed fusion," *Optics and Laser Technology*, vol. 113, pp. 15–26, 2019, doi: 10.1016/j.optlastec.2018.12.005.

[21] R. Morgan, C. J. Sutcliffe, and W. O'Neill, "Experimental investigation of nanosecond pulsed Nd: YAG laser re-melted pre-placed powder beds," *Rapid Prototyping Journal*, vol. 7, no. 3, pp. 159–172, 2001, doi: 10.1108/13552540110395565.

[22] X. Ding, L. Wang, and S. Wang, "Comparison study of numerical analysis for heat transfer and fluid flow under two different laser scan patterns during selective laser melting," *Optik*, vol. 127, no. 22, pp. 10898–10907, 2016, doi: 10.1016/j.ijleo.2016.08.123.

[23] S. Li, H. Xiao, K. Liu, W. Xiao, Y. Li, X. Han, J. Mazumder, and L. Song, "Melt-pool motion, temperature variation and dendritic morphology of Inconel 718 during pulsed- and continuous-wave laser additive manufacturing: A comparative study," *Materials & Design*, vol. 117, pp. 126–135, 2017, doi: 10.1016/j.matdes.2017.01.065.

[24] T. Ullsperger, D. Liu, B. Yürekli, G. Matthäus, L. Schade, B. Seyfarth, H. Kohl, R. Ramm, M. Rettenmayr, and S. Nolte, "Ultra-short pulsed laser powder bed fusion of Al-Si alloys: Impact of pulse duration and energy in comparison to continuous wave excitation," *Additive Manufacturing*, vol. 46, 2021, Art. no. 102085, doi: 10.1016/j.addma.2021.102085.

[25] T. Laag, T. M. Winkel, L. Jauer, D. Heußen, and C. L. Haefner, "Improvement of part accuracy by combination of pulsed wave (PW) and continuous wave (CW) laser powder bed fusion," *Berg Huettenmaenn Monatsh*, vol. 167, no. 7, pp. 308–317, 2022, doi: 10.1007/s00501-022-01235-1.

[26] C. Guo, Y. Zhou, X. Li, X. Hu, Z. Xu, E. Dong, Q. Zhu, and R. M. Ward, "A comparing study of defect generation in IN738LC superalloy fabricated by laser powder bed fusion: Continuous-wave mode versus pulsed-wave mode," *Journal of Materials Science & Technology*, vol. 90, pp. 45–57, 2021, doi: 10.1016/j.jmst.2021.03.006.

[27] K. Georgilas, R. H. U. Khan, and M. E. Kartal, "The influence of pulsed laser powder bed fusion process parameters on Inconel 718 material properties," *Materials Science & Engineering A*, vol. 769, 2020, Art. no. 138527, doi: 10.1016/j.msea.2019.138527.

[28] J. Grünewald, J. Reinelt, H. Sedlak, and K. Wudy, "Support-free laser-based powder bed fusion of metals using pulsed exposure strategies," *Progress in Additive Manufacturing*, vol. 8, no. 3, pp. 123–138, 2023, doi: 10.1007/s40964-023-00429-4.

[29] S. M. H. Hojjatzadeh, Q. Guo, N. D. Parab, M. Qu, L. I. Escano, K. Fezzaa, W. Everhart, T. Sun, and L. Chen, "In-Situ characterization of pore formation dynamics in pulsed wave laser powder bed fusion," *Materials*, vol. 14, no. 11, p. 2936, 2021, doi: 10.3390/ma14112936.

[30] J. Grünewald, P. Clarkson, R. Salveson, G. Fey, and K. Wudy, "Influence of pulsed exposure strategies on overhang structures in powder bed fusion of Ti6Al4V using laser beam," *Metals*, vol. 11, no. 7, p. 1125, 2021, doi: 10.3390/met11071125.

[31] K. Karami, A. Blok, L. Weber, S. M. Ahmadi, R. Petrov, K. Nikolic, E. V. Borisov, S. Leeflang, C. Ayas, A. A. Zadpoor, M. Mehdipour, E. Reinton, and V. A. Popovich, "Continuous and pulsed selective laser melting of Ti6Al4V lattice structures: Effect of post-processing on microstructural anisotropy and fatigue behaviour," *Additive Manufacturing*, vol. 36, 2020, Art. no. 101433, doi: 10.1016/j.addma.2020.101433.

[32] P. Ninpetch, P. Chalermkarnnon, and P. Kowitwarangkul, "Multiphysics simulation of thermal-fluid behavior in laser powder bed

fusion of H13 steel: Influence of layer thickness and energy input," *Metals and Materials International*, vol. 29, pp. 536–551, 2023, doi: 10.1007/s12540-022-01239-z

[33] M. Bayat, V. K. Nadimpalli, and J. H. Hattel, "Multiphysics simulation of thermal and fluid dynamics phenomena during the pulsed laser powder bed fusion process of 316-L steel," in *the 17th UK Heat Transfer Conference (UKHTC2021)*, Apr. 2022, pp. 1–6.

[34] X. Shan, Z. Pan, M. Gao, L. Han, J.-P. Choi, and H. Zhang, "Multi-Physics modeling of melting-solidification characteristics in laser powder bed fusion process of 316L stainless steel," *Materials*, vol. 17, no. 4, p. 946, 2024, doi: 10.3390/ma17040946.

[35] W. Wang, W. Lin, R. Yang, Y. Wu, J. Li, Z. Zhang, and Z. Zhai, "Mesoscopic evolution of molten pool during selective laser melting of superalloy Inconel 738 at elevating preheating temperature," *Materials & Design*, vol. 213, 2022, Art. no. 110355, doi: 10.1016/j.matdes. 2021.110355.

[36] H. Li, X. Liang, Y. Li, and F. Lin, "Performance of high-layer-thickness Ti6Al4V fabricated by electron beam powder bed fusion under different accelerating voltage values," *Materials*, vol. 15, no. 5, p. 1878, 2022, doi: 10.3390/ma15051878.

[37] B. Cheng, X. Li, C. Tuffile, A. Ilin, H. Willeck, and U. Hartel, "Multi-Physics modeling of single-track scanning in selective laser melting: Powder compaction effect," in *Proceedings of the 29th Annual International Solid Freeform Fabrication Symposium – An Additive Manufacturing Conference*, 2018, pp. 1887–1902.

[38] A. Laazizi, B. Courant, F. Jacquemin, and H. Andrzejewski, "Applied multi-pulsed laser in surface treatment and numerical–experimental analysis," *Optics & Laser Technology*, vol. 43, no. 7, pp. 1257–1263, 1997, doi: 10.1016/ j.optlastec.2011.03.019.

[39] W. Yan, W. Ge, Y. Qian, S. Lin, B. Zhou, G. J. Wagner, F. Lin, and W. K. Liu, "Multi-Physics modeling of single/multiple-track defect mechanisms in electron beam selective melting," *Acta Materialia*, vol. 137, pp. 214–224, 2017, doi: 10.1016/j.actamat.2017.08.033.

[40] C. Tang, J. L. Tan, and C. H. Wong, "A numerical investigation on the physical mechanisms of single track defects in selective laser melting," *International Journal of Heat and Mass Transfer*, vol. 126, pp. 957–968, 2018, doi: 10.1016/j.ijheatmasstransfer.2018.06.073.

[41] J. Ding, P. Colegrove, J. Mehnen, S. Ganguly, P. M. Sequeira Almeida, F. Wang, and S. Williams, "Thermo-mechanical analysis of wire and arc additive layer manufacturing process on large multi-layer parts," *Computational Materials Science*, vol. 50, pp. 3315–3322, 2011, doi: 10.1016/j.commatsci.2011.06.023.

[42] K. C. Mills, *Recommended Values of Thermophysical Properties for Selected Commercial Alloys*. Cambridge, UK: Woodhead Publishing, 2002.

[43] M.-S. Pham, B. Dovgyy, P. A. Hooper, C. M. Gourlay, and A. Piglione, "The role of side-branching in microstructure development in laser powder-bed fusion," *Nature Communications*, vol. 11, no. 749, 2020, doi: 10.1038/s41467-020-14453-3.

[44] A. K. Ball and A. Basak, "AI modeling for high-fidelity heat transfer and thermal distortion forecast in metal additive manufacturing," *The International Journal of Advanced Manufacturing Technology*, vol. 128, pp. 2995–3010, 2023, doi: 10.1007/s00170-023-11974-1.

[45] Z. Zhang, T. Zhang, C. Sun, S. Karna, and L. Yuan, "Understanding melt pool behavior of 316L stainless steel in laser powder bed fusion additive manufacturing," *Micromachines*, vol. 15, no. 2, p. 170, 2024, doi: 10.3390/mi15020170.

[46] M. Cheng, X. Zou, Y. Pan, Y. Zhou, W. Liu, and L. Song, "Residual stress control using process optimization in directed energy deposition," *Materials*, vol. 16, no. 19, p. 6610, 2023, doi: 10.3390/ma16196610.

[47] T. Rautio, J. Jalava-Kanervio, J. Kumpula, J. Mäkikangas, and A. Järvenpää, "Microstructure and mechanical properties of laser butt welded laser powder bed fusion manufactured and sheet metal 316L parts," *Key Engineering Materials*, vol. 861, pp. 9–14, 2020, doi: 10.4028/ www.scientific.net/KEM.861.9.

[48] B. E. Kashyap and K. Tangri, "Grain growth behaviour of type 316L stainless steel," *Materials Science and Engineering: A*, vol. 149, pp. L13–L16, 1992, doi: 10.1016/0921-5093(92) 90392-E.

[49] J. Bliedtner, H. Müller, and A. Barz, *Lasermaterialbearbeitung: Grundlagen* –

Verfahren – Anwendungen – Beispiele. Leipzig, Germany: *Fachbuchverlag Leipzig*, 2013.

[50] H. Yin, J. Yang, R. D. Fischer, Z. Zhang, B. Prorok, L. Yuan, and X. Lou, "Pulsed laser additive manufacturing for 316L stainless steel: A new approach to control subgrain cellular structure," *JOM*, vol. 75, no. 12, pp. 5027–5036, 2023, doi: 10.1007/s11837-023-06177-8.

[51] Z. Rui, J. Liu, and Y. Shi, "Influence of laser mode on size effect in manufacturing AlSi10Mg mini structures by laser powder bed fusion technology," *Optics and Laser Technology*, vol. 181, 2025, Art. no. 111748, doi: 10.1016/j.optlastec.2024.111748.

[52] P. Nogueira, D. C. Silva, A. P. Serro, P. Lopes, L. Oliveira, J. L. Alves, L. Reis, J. Magrinho, C. Santos, M. J. Carmezim, R. A. Cláudio, A. M. Deus, M. B. Silva, and M. F. Vaz, "Evaluation of the roughness of lattice structures of AISI 316L stainless steel produced by laser powder bed fusion," *Engineering Manufacturing Letters*, vol. 2, no. 1, pp. 39–44, 2024, doi: 10.24840/2795-5168_002-001_2682.

[53] C. Tang, K. Q. Le, and C. H. Wong, "Physics of humping formation in laser powder bed fusion," *International Journal of Heat and Mass Transfer*, vol. 149, Mar. 2020, Art. no. 119172, doi: 10.1016/j.ijheatmasstransfer.2019.119172.

[54] E. Assuncao, S. Williams, and D. Yapp, "Interaction time and beam diameter effects on the conduction mode limit," *Optics and Lasers in Engineering*, vol. 50, no. 6, pp. 823–828, 2012, doi: 10.1016/j.optlaseng.2012.02.001.

[55] T. Qi, H. Zhu, H. Zhang, J. Yin, L. Ke, and X. Zeng, "Selective laser melting of Al7050 powder: Melting mode transition and comparison of the characteristics between the keyhole and conduction mode," *Materials & Design*, vol. 134, pp. 334–347, 2017, doi: 10.1016/j.matdes.2017.09.014.

[56] Y. Xu, Y. Zhang, X. Li, Y. Zhong, K. Lin, B. Liao, X. Guo, C. Yuan, and S. Zhang, "Single-track investigation of additively manufactured mold steel with larger layer thickness processing: Track morphology, melt pool characteristics and defects," *Optics & Laser Technology*, vol. 171, 2024, Art. no. 110378, doi: 10.1016/j.optlastec.2023.110378.

[57] J. Pou, A. Riveiro, and P. Davim, *Additive Manufacturing*. Amsterdam, Netherlands: *Elsevier*, 2021.

[58] L'. Kaščák, J. Varga, J. Bidulská, and R. Bidulský, "Simulation of 316L stainless steel produced by the laser powder bed fusion process," *Materials*, vol. 16, no. 24, p. 7653, Dec. 2023, doi: 10.3390/ma16247653.

[59] W. Wang, H. Garmestani, and S. Y. Liang, "Prediction of upper surface roughness in laser powder bed fusion," *Metals*, vol. 12, no. 1, p. 11, 2021, doi: 10.3390/met12010011.